Supporting Information

Great Enhancements in Thermoelectric Power Factor of BiSbTe Nanostructured Films with Well-Ordered Interfaces

Hsiu-Cheng Chang,[a] Chun-Hua Chen[†], and Yung-Kang Kuo[‡,b]*

[†]Department of Materials Science and Engineering, National Chiao Tung University
  1001 Ta-Hsueh Rd., Hsin-Chu, 30010 Taiwan, R.O.C.

[‡]Department of Physics, National Dong Hwa University
  No. 1, Sec. 2, Da Hsueh Rd., Shoufeng, Hualien, 97401, Taiwan, R.O.C.

E-mail address: [†],*ChunHuaChen@mail.nctu.edu.tw; [‡],*ykkuo@mail.ndhu.edu.tw

Table of Contents

Morphologies, XRD patterns, SEM compositions and room-temperature thermoelectric properties: The series of (015) oriented $Bi_{0.4}Sb_{1.6}Te_3$ nanocolumns
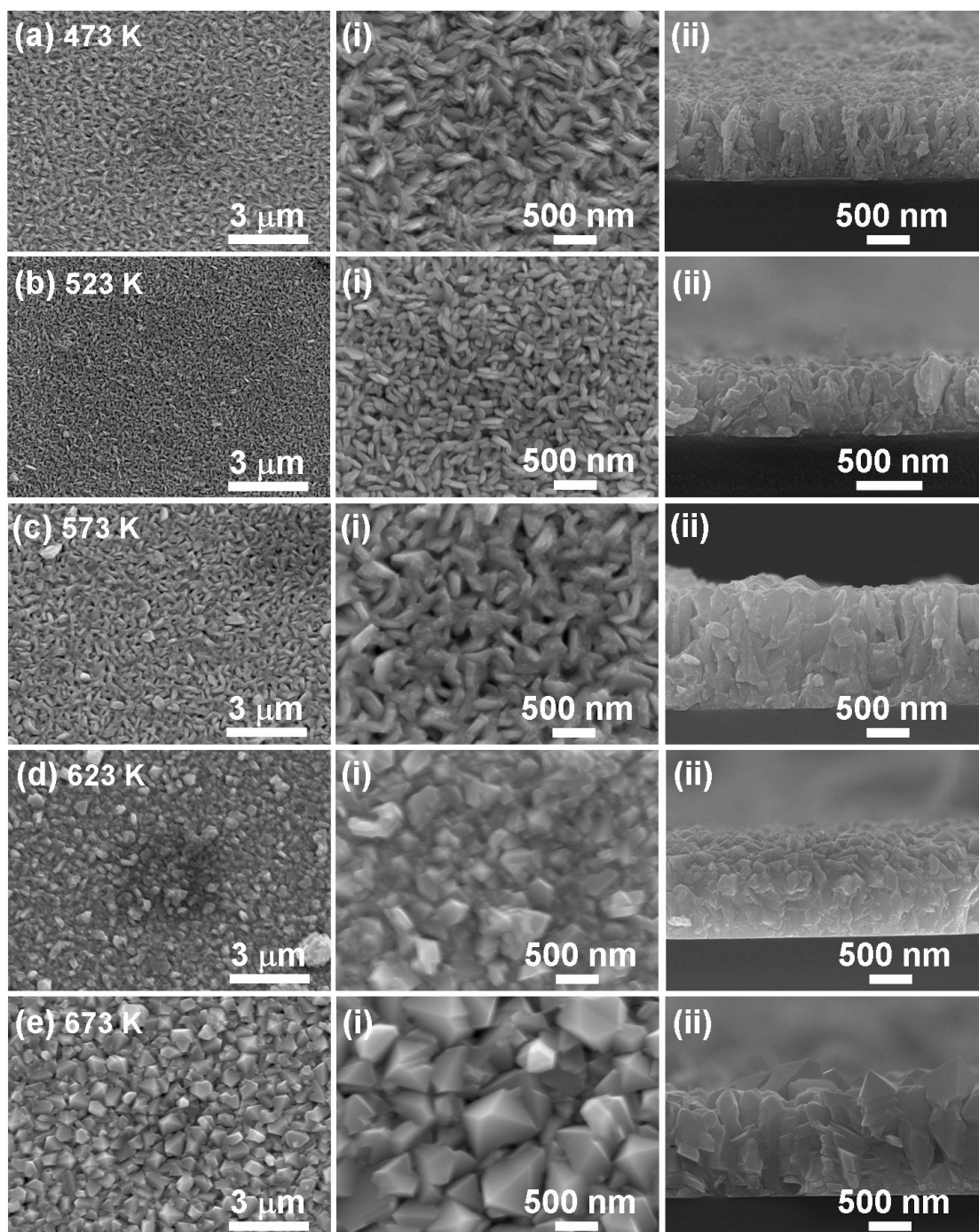
Figure S1 show the top-view SEM images of a series of uniform and large-area $Bi_xSb_{2-x}Te_3$ nanostructures deposited at various substrate temperatures from 473 to 673 K under an Ar ambient pressure of 0.09 torr for 3 h. From the magnified top-view and cross-sectional SEM images as respectively shown in Figure S1(i) and S1(ii), all the morphologies present column structures perpendicular to the substrate surface. The film thickness is 830, 500, 1300, 1100, and 1250 nm for 473, 523, 573, 623, and 673 K, respectively.

Figure S2(a) shows the XRD patterns recorded with a symmetrical θ-2θ geometry. As can be seen, all the diffracted peaks of the prepared nanocolumns can be indexed with bulk $Bi_{0.4}Sb_{1.6}Te_3$ (JCPDS 65-3674). Additionally, a clear (015) preferential orientation is found for all the specimens by quantitatively analyzing the integrated intensity of the reflections. According to the SEM-EDX analyses displayed in Figure S2(b), the Bi content slightly decreases with the temperature increase.

Figure S3 shows a series of electrical and thermoelectric properties measured at room temperature. All the $Bi_{0.4}Sb_{1.6}Te_3$ nanocolumns exhibit positive Hall coefficients, indicating that the hole-type carriers dominate the transport properties. As can be found in Figure S3(a), a higher carrier mobility is observed as the temperature increases, which may originate from the improved film crystallinity. The electrical conductivity independently measured by a four-probe technique (CMT SR2000N) is 38, 64, 69, 73, and 315 Scm^{-1} (see Figure S3(b)) for nanocolumns deposited at 473, 523, 573, 623, and 673 K, respectively. As shown in Fig. S1, when the substrate temperature increases, the grains of the deposited film become larger and the film structure also becomes denser with less defects. Such structural tendencies with increasing temperature equal to the reduction of the boundary scattering for both electrons and phonons, and are thus actually helpful for improving the electrical conductivity. The corresponding I-V curves shown in Figure S3(e) exhibit an excellent linear relationship over

the entire voltage range applied, indicating the ohmic contacts. It is noted that the measured electrical conductivity shows a great resemblance to the mobility against the deposition temperature, suggesting that the electrical transport in these BiSbTe films is dominated by the carrier mobility.

The positive Seebeck coefficients as displayed in Figure S3(c) and S3(f) confirm the p-type semiconducting behaviors for all specimens. The small contribution from the electrical leads (Cu wires) has been carefully subtracted for the present Seebeck coefficients. A strong deposition-temperature dependence of the Seebeck coefficient is found where the value is 120, 149, 188, 204, and 213 μVK^{-1} for 473, 523, 573, 623, and 673 K, respectively. In the present series of (015) oriented nanocolumns, the specimen deposited at 673 K has the highest power factor (~14.34 $\mu Wcm^{-1}K^{-2}$) as shown in Figure S3(d), which probably originates from a relatively higher Sb content as well as a better crystallinity. As concluded, the deposition temperature not only dominates the nanostructures but also plays an important role in influencing the composition and thus further affects the thermoelectric properties.

Figure S1. (a)-(e) The top-view SEM images of the (015) oriented $Bi_{0.4}Sb_{1.6}Te_3$ nanocolumns

deposited at 473, 523, 573, 623, and 673 K, respectively. The magnified (i) top-view and (ii)

cross-sectional SEM images are shown along with (a)-(e).
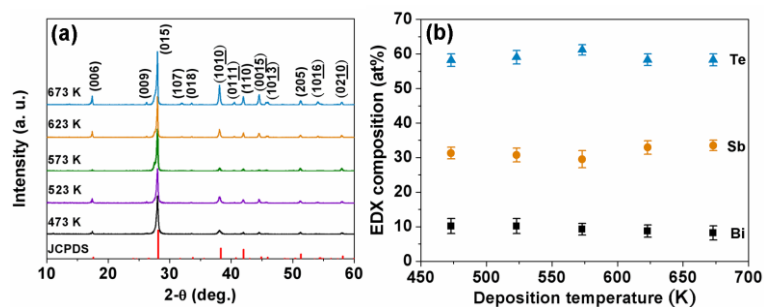
Figure S2. (a) X-ray diffraction patterns recorded from the (015) oriented $Bi_{0.4}Sb_{1.6}Te_3$ nanocolumns deposited at 473, 523, 573, 623, and 673 K. (b) The SEM-EDX compositions as a function of the deposition temperature.
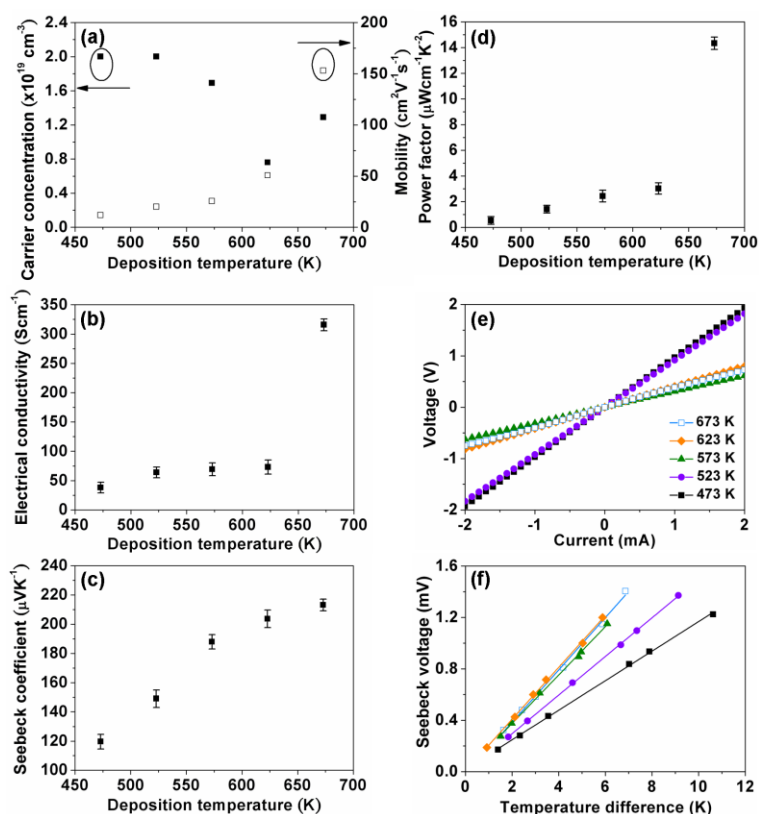
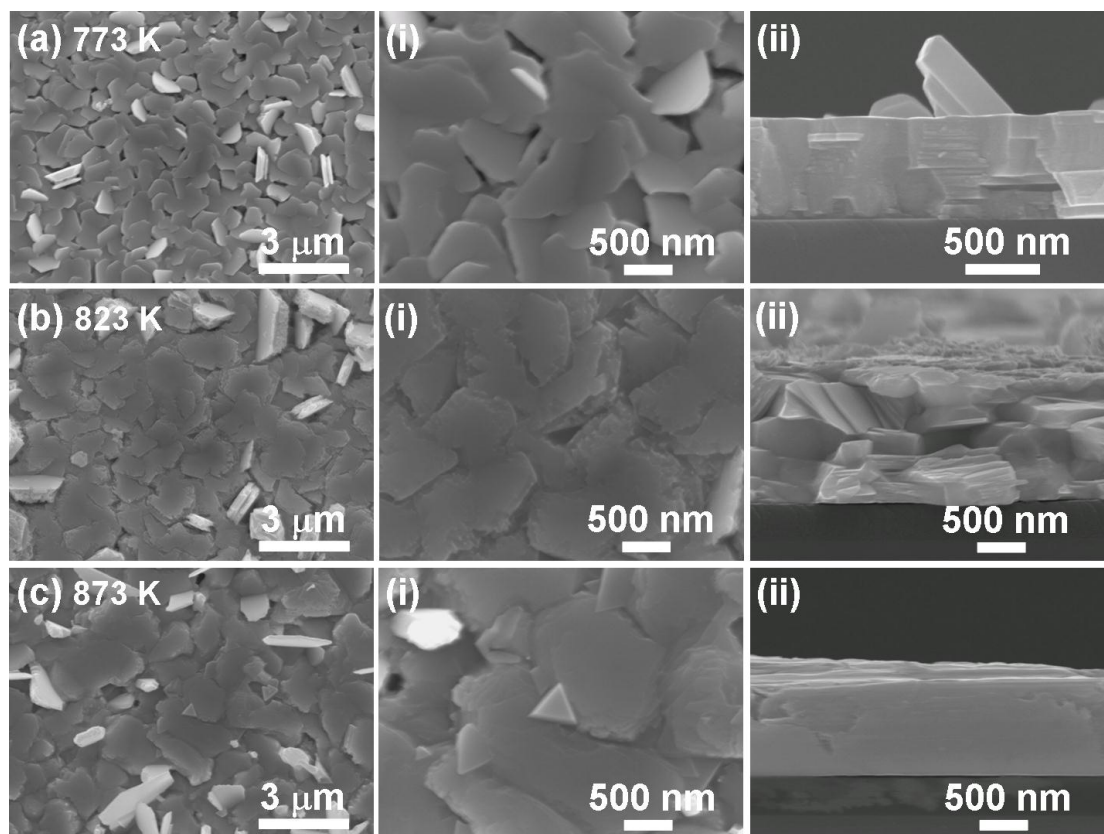**Figure S3.** (a) The carrier concentration and mobility, (b) the electrical conductivity, (c) the Seebeck coefficient, and (d) the power factor measured at room temperature as functions of the deposition temperatures for obtaining (015) oriented nanocolumns. The corresponding I-V curves and the plots of the Seebeck voltage versus the temperature difference created are respectively shown in (e) and (f).

Morphologies, XRD patterns, SEM compositions and room-temperature thermoelectric properties: The series of (001) oriented $Bi_{0.5}Sb_{1.5}Te_3$ nanodiscs

Figure S4(a)-(e) show the top-view SEM images of a series of uniform and large-area $Bi_xSb_{2-x}Te_3$ nanostructures deposited at 773, 823, and 873 K under an Ar ambient pressure of 0.15 torr for 3 h. In the present series, the disc-like orderly structures, lying on the substrates, are clearly observed (see Figure S4(i)) and the continuity and regularity of the stacks of discs is improved as the deposition temperature increases (see Figure S4(ii)). The film thickness are 690, 1300, and 1100 nm for 773, 823, and 873 K, respectively.

The XRD patterns shown in Figure S5(a) can be correspondingly indexed with the $Bi_{0.4}Sb_{1.6}Te_3$ (JCPDS 65-3674) in which a slight peak shift toward a lower angle is found, mainly due to the higher Sb fraction of the present nanodiscs, compared with the above nanocolumns, as will also be quantitatively realized in the following SEM-EDX measurement. Moreover, an obvious (001) preferential orientation can also be found for all specimens from the only presence of (00l) basal-planes. Figure S5(b) confirms that the nanodiscs deposited at 773, 823, and 873 K have a similar composition of Bi:Sb:Te = 10:30:60. Similar to previous series, the positive Hall coefficients for these three specimens suggest that the hole-type carrier should dominate the thermoelectric properties. From Figure S6(a), the nanodiscs prepared at 873 K (7.7×10^{-19} cm^{-3}) display a higher carrier concentration than those prepared at 773 K (2.9×10^{-19} cm^{-3}) and 823 K (1.5×10^{-19} cm^{-3}). Furthermore, the nanodiscs deposited at 773, 823, and 873 K, respectively, exhibit a high electrical conductivity of 1050, 861, and 1441 Scm^{-1} which approaches the value of the nanostructured bulk (1280 Scm^{-1}) [1] (see Figure S6(b)). A contributory factor to the higher electrical conductivity observed from the specimen deposited at 873 K is most likely due to its stronger (00l) orientation. Although the nanodiscs show comparable high electrical conductivities, their values of Seebeck coefficient only reach 50% ~ 70% (97~130 μVK^{-1}) of the bulk (185 μVK^{-1})[1] as shown in Figure S6(c). Compared

with the case of nanocolumns, the Seebeck coefficients of the nanodiscs exhibit an inverse tendency as the deposition temperature increases, probably due to the slight deficiency of Sb as part of Sb is in the vapor form at such high deposition temperatures. As a result (Figure S6(d)), the (001) oriented nanodiscs deposited at 773 K (17.75 $\mu Wcm^{-1}K^{-2}$) exhibit a higher power factor than that prepared at 823 K (8.87 $\mu Wcm^{-1}K^{-2}$) and 873 K (13.45 $\mu Wcm^{-1}K^{-2}$).



Figure S4. (a)-(c) The top-view SEM images of the (001) oriented $Bi_{0.5}Sb_{1.5}Te_3$ nanodiscs deposited at 773, 823, and 873 K, respectively. The magnified (i) top-view and (ii) cross-sectional SEM images are shown along with (a)-(c).

8
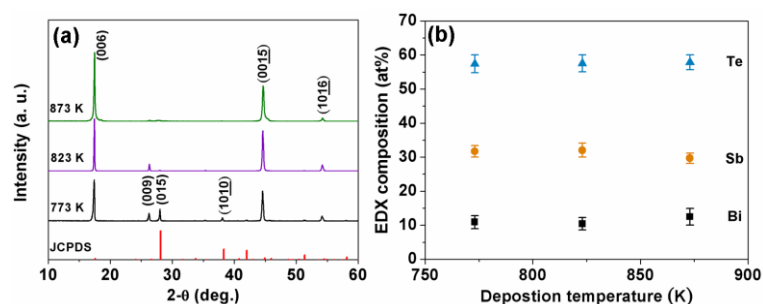
Figure S5. (a) X-ray diffraction patterns recorded from the (001) oriented $Bi_{0.5}Sb_{1.5}Te_3$ nanodiscs prepared at 773, 823, and 873 K. (b) The SEM-EDX compositions as a function of the deposition temperature.
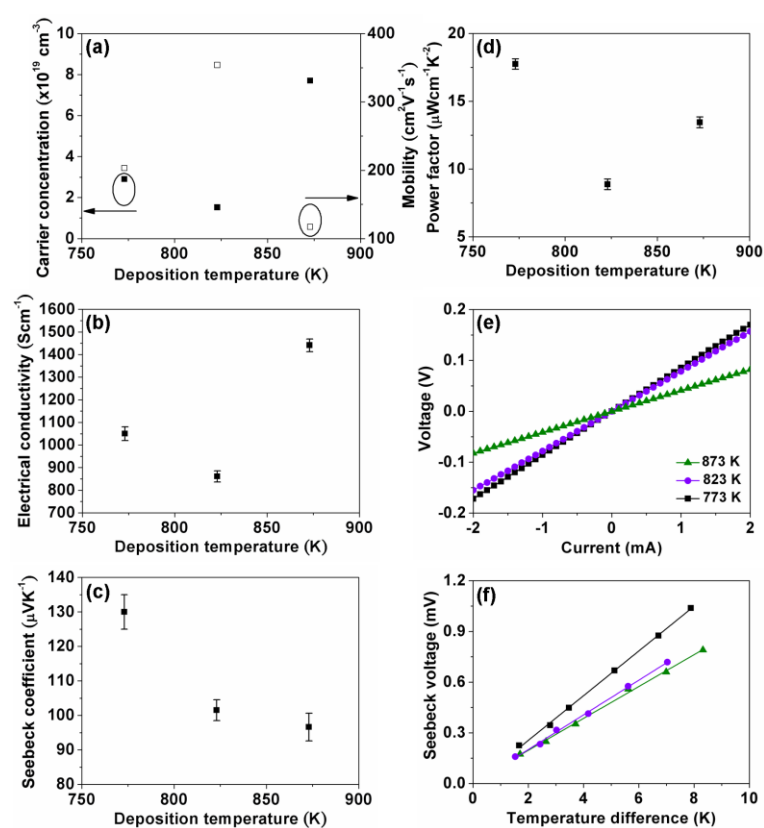
**Figure S6**. (a) The carrier concentration and mobility, (b) the electrical conductivity, (c) the Seebeck coefficient, and (d) the power factor measured at room temperature as functions of the deposition temperatures for obtaining (001) oriented $Bi_{0.5}Sb_{1.5}Te_3$ nanodiscs. The corresponding I-V curves and the plots of the Seebeck voltage versus the temperature difference created are respectively shown in (e) and (f).

Morphologies, XRD patterns, SEM compositions and room-temperature thermoelectric properties: The series of (001) and (015) doubly oriented $Bi_{0.5}Sb_{1.5}Te_3$ nanodiscs and $Bi_{0.7}Sb_{1.3}Te_3$ nanolayers

Figure S7 represents the disc- and layer-like structures respectively prepared at 723 K (~0.11 torr) and 883 K (~0.4 torr). The XRD patterns shown in Figure S8(a) can be correspondingly indexed with bulk $Bi_{0.4}Sb_{1.6}Te_3$, where a distinct doubly preferential orientation of (001) and (015) is clearly found after quantitatively analyzing the integrated intensities of the diffracted peaks. Figure S8b reveals that the stoichiometric ratios of the specimens obtained at 723 K and 883 K are Bi:Sb:Te = 10:30:60 and Bi:Sb:Te = 13:27:60, respectively. In comparison with the deposition map of the nanodiscs described previously as well as the present series, the nanodiscs deposited at 723 K and 773 K show a similar morphology and composition, but a very different preferential orientation, probably because of the difference in ambient pressure. Similarly, Russo et al.[2] have demonstrated that Bi_2Te_3 films prepared by PLD process at 620 K with a higher deposition pressure of ~1.5 torr show a double orientation of (00l) and (015), indicating the ambient pressure indeed plays an important role for obtaining such a double preferential orientation. Additionally, the SZM model[3] also addresses that a higher argon pressure can limit the mobility of adatoms and thus permit some specific crystal structures.

Figure S9(a) shows positive Hall coefficients, indicating that the hole-type carriers dominate the thermoelectric properties. The carrier concentration of the nanolayers (~2.4×10^{20} cm^{-3}) is one order of magnitude higher than that of the nanodiscs prepared at 723 K (~2.3×10^{19} cm^{-3}), but the mobility is ~35% lower than that of the nanodiscs (177 $cm^2V^{-1}s^{-1}$). Thus, the electrical conductivity of nanolayers (2713 Scm^{-1}) is more than four times higher than that of the nanodiscs (651 Scm^{-1}), as seen in Figure S9(b). The linear I-V curves over the entire range of the applied voltages suggest the ohmic contacts. The resistances of the

10

nanodiscs and nanolayers deposited at 723 K and 883 K are 177 Ω and 114 Ω, respectively. The positive Seebeck coefficients also suggest the p-type semiconducting behavior which is consistent with the Hall results. Besides, the $Bi_{0.5}Sb_{1.5}Te_3$ nanodiscs (195 μVK^{-1}) show a higher Seebeck coefficient compared with the $Bi_{0.7}Sb_{1.3}Te_3$ nanolayers (97 μVK^{-1}), as can be seen in Figure S9(c). This result indicates that the Seebeck coefficient for the doubly oriented cases decreases with the increase in deposition temperature. Such tendency is similar to the (001) oriented series probably due to the dissipation of Sb at higher temperatures. It is worth noting that both doubly oriented nanodiscs (24.82 $\mu Wcm^{-1}K^{-2}$) and nanolayers (25.58 $\mu Wcm^{-1}K^{-2}$), respectively, deposited at 723 K and 883 K show higher power factors than specimens with single orientation of either (015) or (001).
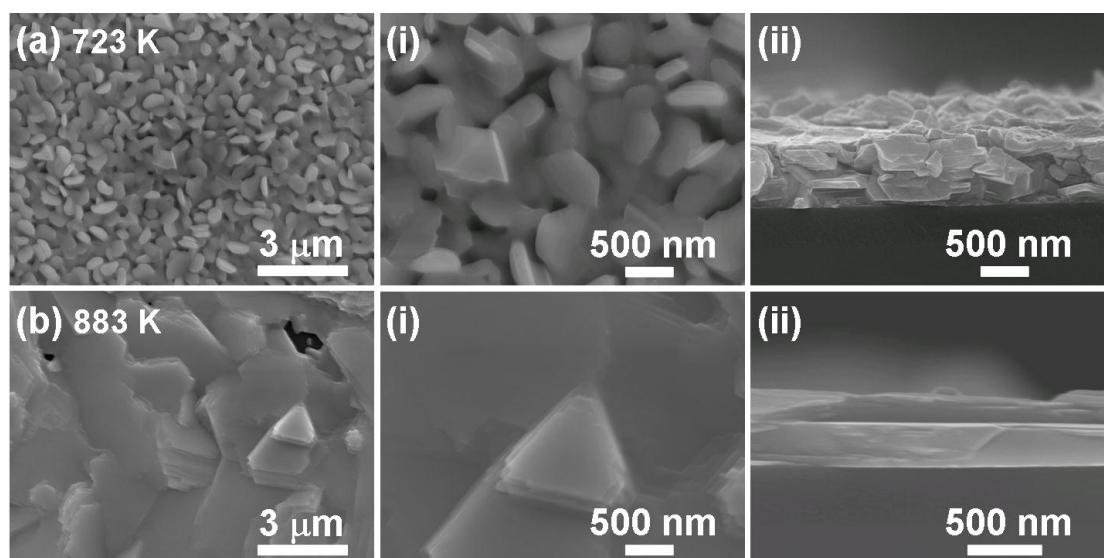
Figure S7. (a) and (b) The top-view SEM images of the (00l) and (015) doubly oriented $Bi_{0.5}Sb_{1.5}Te_3$ nanodiscs and $Bi_{0.7}Sb_{1.3}Te_3$ nanolayers deposited at 723 K and 883 K, respectively. The magnified (i) top-view and (ii) cross-sectional SEM images are shown along with (a) and (b).
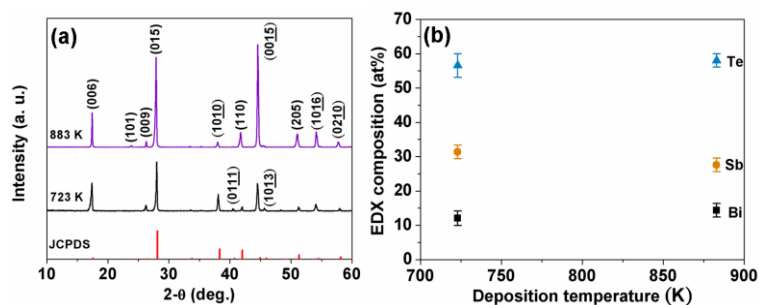
Figure S8. (a) X-ray diffraction patterns recorded from the (00l) and (015) doubly oriented $Bi_{0.5}Sb_{1.5}Te_3$ nanodiscs and $Bi_{0.7}Sb_{1.3}Te_3$ nanolayers. (b) EDX compositions as a function of the deposition temperatures.
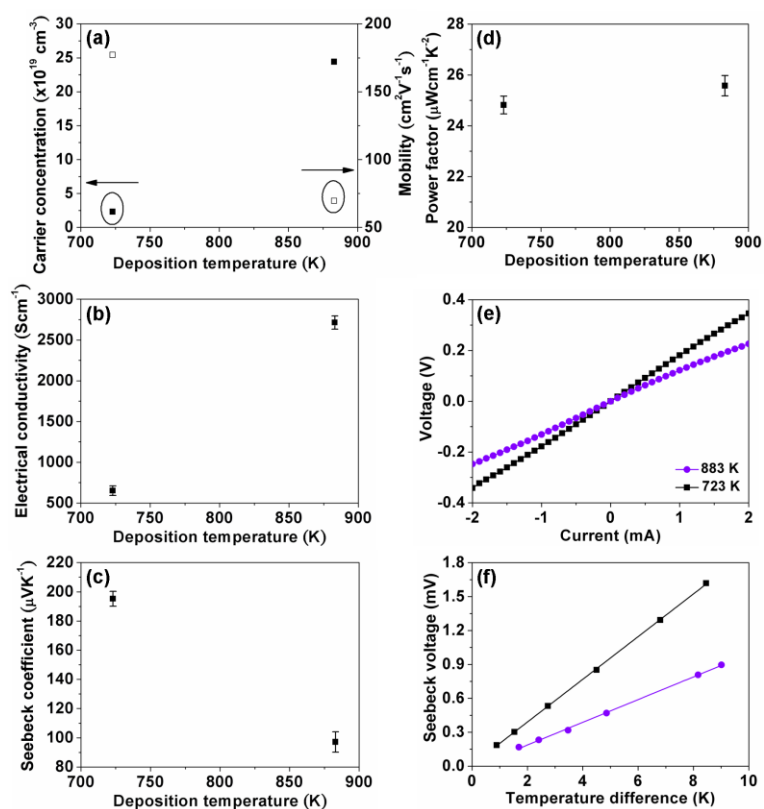
Figure S9. (a) The carrier concentration and mobility, (b) the electrical conductivity, (c) the Seebeck coefficient, and (d) the power factor measured at room temperature as functions of the deposition temperatures for obtaining the (00l) and (015) doubly oriented $Bi_{0.5}Sb_{1.5}Te_3$ nanodiscs and $Bi_{0.7}Sb_{1.3}Te_3$ nanolayers. The corresponding I-V curves and the plots of the Seebeck voltage versus the temperature difference created are respectively shown in (e) and (f).

12

XPS and TEM-EDX spectra of the most outstanding specimens selected from these three series of $Bi_xSb_{2-x}Te_3$ nanostructures

By carefully examining the above results, we can conclude that higher electrical conductivity will simultaneously lead to a higher power factor for the present oriented $Bi_xSb_{2-x}Te_3$ nanostructures and thus a potentially higher performance of the thermoelectric devices might be expected by applying these featured $Bi_xSb_{2-x}Te_3$ nanostructures. To understand the fundamentals of the high electrical conductivity observed in the present numerous $Bi_xSb_{2-x}Te_3$ nanostructures, we specially selected the three most outstanding specimens for further analyses. For alloyed $Bi_xSb_{2-x}Te_3$, the composition is one of the most important factors that effectively affects the thermoelectric properties. Therefore, although SEM-EDX has been performed to clarify the composition from a large area, we also analyzed the composition from a very local region of pieces cut from the oriented films by TEM-EDX. Figure S10(a)-(c) shows the cross-sectional TEM images of the selected $Bi_xSb_{2-x}Te_3$ nanostructures with a (015), (00l), and a double (00l) and (015) orientation. The corresponding TEM-EDX spectra shown in Figure S10(d)-(f) reveal that the composition is $Bi_{0.4}Sb_{1.6}Te_3$, $Bi_{0.5}Sb_{1.5}Te_3$, and $Bi_{0.7}Sb_{1.3}Te_3$, respectively.

Surface oxidation is always a serious problem for metallic self-assembled nanostructures because of their high surface-to-volume ratio, which will cause severe deterioration in the electrical conductivity and consequently inhibit thermoelectric ZTs in practical applications. The XPS results of $Bi_{0.4}Sb_{1.6}Te_3$, $Bi_{0.5}Sb_{1.5}Te_3$, and $Bi_{0.7}Sb_{1.3}Te_3$ nanostructures, which were respectively deposited at 673, 773, and 883 K, are shown in Figure S11. All the recorded spectra were corrected by external Pt signals to prevent the charge effect. No significant changes were found in the profiles of the Bi, Sb, and Te bands between these three alloyed specimens. The Bi $4f_{7/2}$ and $4f_{5/2}$ bands which locate at 157.2 and 162.6 eV (see Figure S11(a)) are rather symmetrical, while non-linear backgrounds are considered and have no

high-binding-energy shoulders to combine with, indicating the absence of oxidized states typically located at 158.5 and 163.9 eV, respectively[4]. Regardless of the overlapping of the Sb $3d_{5/2}$ and O 1s which locates at 528.5 eV and 529 eV, respectively, the symmetrical profile and the binding energy of 537.9 eV for the Sb $3d_{3/2}$ peak undoubtedly proves the metallic state of Sb as presented in Figure S11(b). The most affected components are the Te atoms since, no matter the uncapped Bi_2Te_3 nanoparticles[5] or the capped Bi-Sb-Te nanocrystals[4], Te atoms are found to exhibit faster oxidation than Bi and Sb atoms. The Te $3d_{5/2}$ and $3d_{3/2}$ which were respectively located at 572.5 and 583.1 eV[6] clearly indicate the absence of Te oxides with a binding energy of 575.6 and 586.2 eV[4] (see Figure S11(c)).

Based on the above XPS evidence, we concluded that the $Bi_xSb_{2-x}Te_3$ nanostructures prepared by PLD at various substrate temperatures are situated in the alloyed state without the existence of traceable surface oxidation. It is worth emphasizing that the extremely clean surfaces and interfaces are actually the most important essentials because they are the threshold to exploring and developing distinct thermoelectric phenomena in self-assembled nanostructures. In this work, in addition to the oriented high-density twin structures, the absence of surface oxides in the prepared $Bi_xSb_{2-x}Te_3$ nanostructures concretely plays a crucial role in achieving the very low electrical resistivity and thus, as will be discussed in the article, enhances the ZTs.
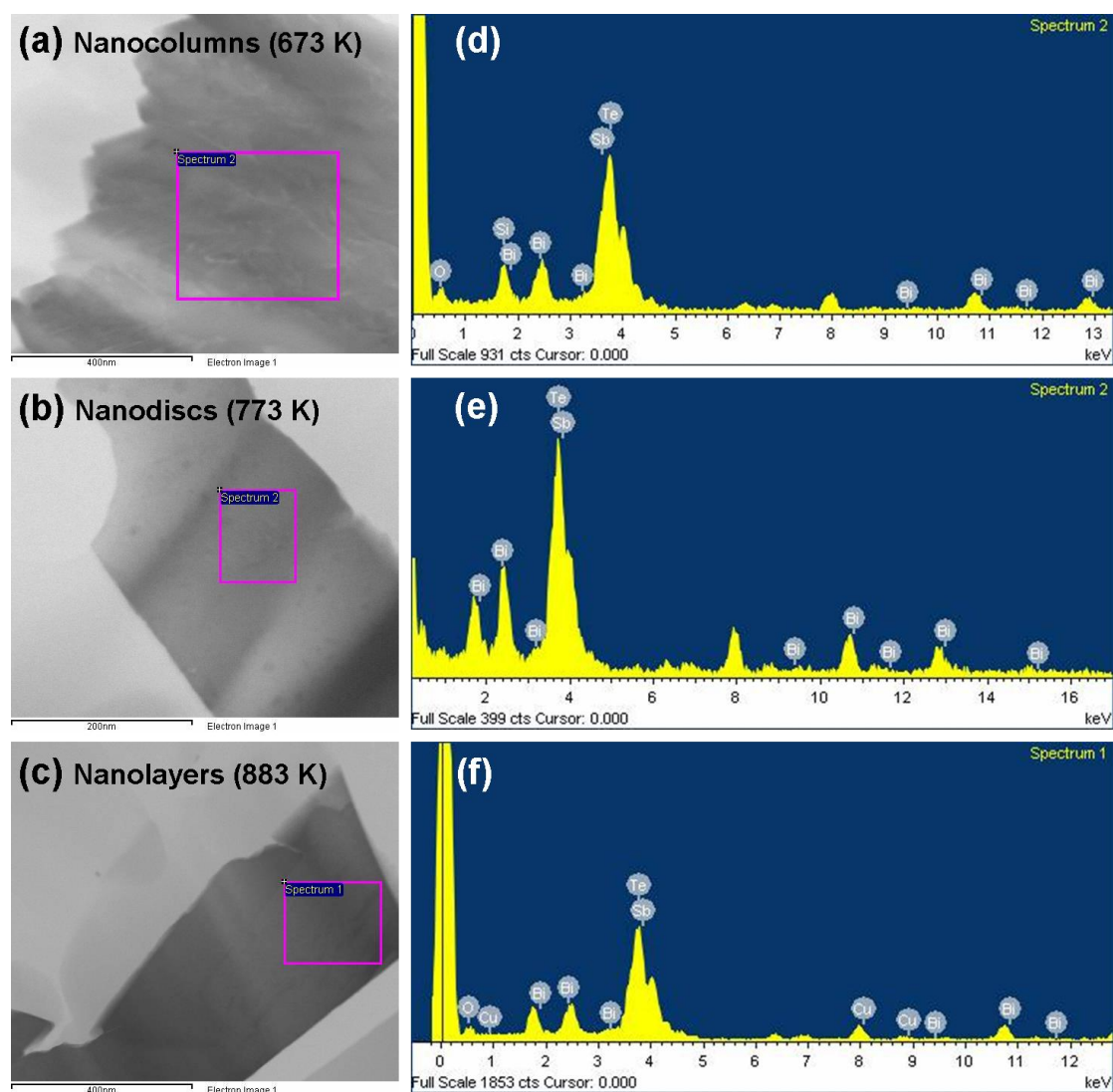
Figure S10. The cross-sectional TEM images of one cut pieces of (a) $Bi_{0.4}Sb_{1.6}Te_3$ nanocolumns, (b) $Bi_{0.5}Sb_{1.5}Te_3$ nanodiscs, and (c) $Bi_{0.7}Sb_{1.3}Te_3$ nanolayers prepared at 673, 773, and 883 K, respectively. The corresponding TEM-EDX spectra are shown in (d)-(f).
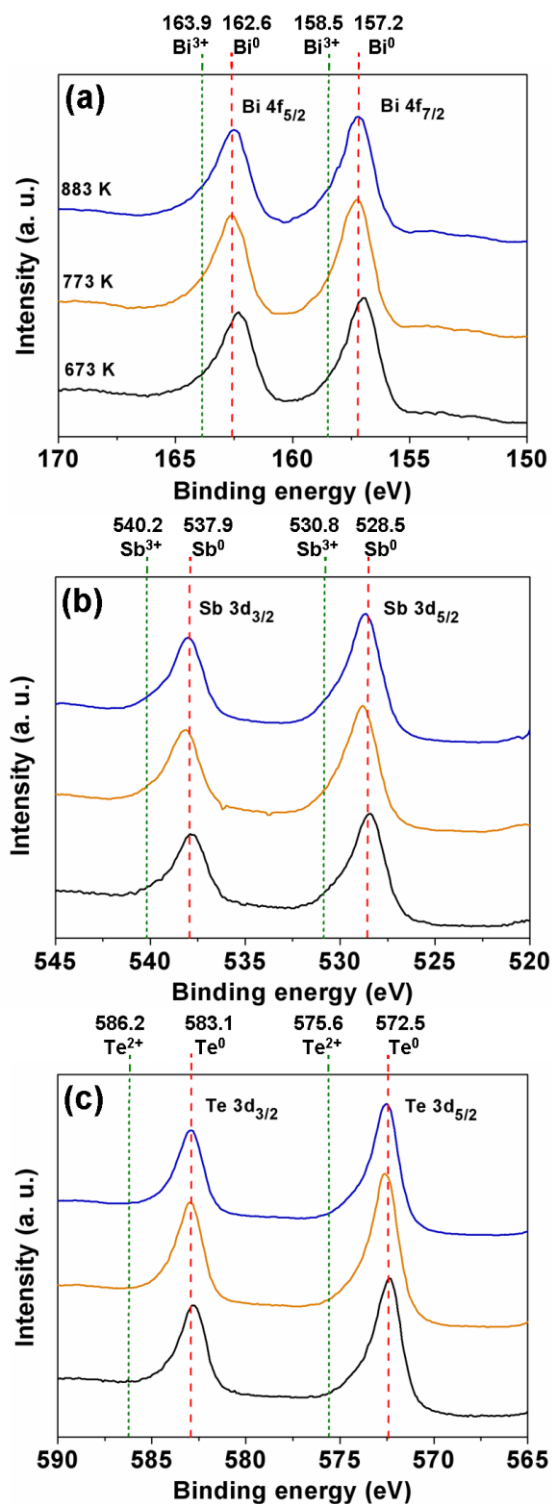
Figure S11. XPS spectra of (a) Bi 4f, (b) Sb 3d, and (c) Te 3d states showing the binding energy of $Bi_{0.4}Sb_{1.6}Te_3$, $Bi_{0.5}Sb_{1.5}Te_3$, and $Bi_{0.7}Sb_{1.3}Te_3$ nanostructures deposited at 673, 773, and 883 K, respectively, and evidence of the absence of the oxidation state; the dashed and dotted lines represent the pure and oxide reference sates of Bi, Sb, and Te, respectively.

Systematically TEM investigations of the most outstanding specimens selected from these

three series of $Bi_xSb_{2-x}Te_3$ nanostructures

High resolution transmission electron microscope (HRTEM) observations were performed to investigate the oriented and twined nanocrystals. Figure S12(a) represents the large-area cross-sectional TEM image of the $Bi_{0.7}Sb_{1.3}Te_3$ nanolayers with a double orientation of (001) and (015) deposited at 883 K in which the dash lines mark the interfaces found in the layers. Figure S12(b)-(d) respectively show the HRTEM images and the corresponding fast Fourier-transform (FFT) electron diffraction (ED) patterns of one selected single domain. The presence of the ($00\underline{15}$), (015), and ($0\bar{1}\underline{10}$) planes indicates a common zone axis of [100] for these regions. Additionally, since all these regions have a ($00\underline{15}$) orientation which is normal to the substrate, we can conclude that (b), (c), and (d) regions exhibit the same in-plane and out-of-plane orientations; in other words, they should belong to one single crystal. However, a closer look at <015> and <015> in Figure S12(b) and S12(d) reveals a mirror symmetrical relationship, obviously indicating the existence of single or multiple basal-plane twin structures parallel to the substrate somewhere in between the (b) and (d) regions. In fact, from their corresponding FFT ED patterns in Figure S12(b) and S12(d), such mirror symmetry can also be clearly found. As expected, from the FFT ED pattern in Figure S12(c) composing spots of mirror structures, it is seen undoubtedly that twin structures formed horizontally in region (c). In region (e), the monotone ($10\bar{5}$) lattice fringes as well as the corresponding FFT ED pattern (zone axis= [$5\bar{5}1$]) indicates that the present region is a single crystal with a different orientation compared with regions (b) to (d). In region (f), the presence of horizontal ($00\underline{15}$) and perpendicular (110) lattice fringes indicates the same out-of-plane orientation but a different in-plane orientation compared with other regions.

In the case of $Bi_{0.5}Sb_{1.5}Te_3$ nanodiscs, similarly, different regions within one domain and across neighboring domains separated by dash lines were selected for HRTEM analyses. From the lattice fringes as well as the vertically dense FFT ED spots shown in Figure S13(b)-(d), numerous twins parallel to the basal planes are evidently found in the whole grain. Again, we can only locate twins in the (001) oriented grains as observed in Figure S12. The slightly elongated diffraction spots suggest the presence of a small misorientation deviating from the perfect alignment between the nanocrystallines in the resulting nanodiscs. The clear interface along two neighboring grains as shown in Figure S13(e) and S13(f) obviously indicates a nonbasal-plane twin boundary. The lattice planes smoothly move from right-side to left-side grain, indicating that the twin boundary has a rather high coherent degree. In region (f), the mismatches between lattice planes across these two domains as indexed evidence a defective twin boundary. We believe that such nonbasal-plane twin boundaries formed between neighboring grains having similar orientations can provide large-area pathways for electron transport and lead to a high electrical conductivity as will be discussed below. In addition, a clear pair of the basal-plane twin boundary was found in Figure S13(g) to form a twin band having a band width of ~3 nm, which is comparable to the lattice constant c of the hexagonal $Bi_xSb_{2-x}Te_3$. The TEM image (Figure S13(a)) showing densely appeared twin bands parallel to the (001) oriented grains around (g) region evidently proves the twins across whole grains to reach the twin boundaries.

As the deposition temperature is lowered to 673 K, the morphology of the $Bi_{0.4}Sb_{1.6}Te_3$ nanostructures is transferred to uniform nanocolumns with pyramidal caps (see Figure 1(a) and 1(d)). The HRTEM images and their corresponding FFT ED patterns shown in Figure S14(b)-(f) reveal a series of parallel lattice fringes, clearly indicating a typical single crystal with the absence of twin structures. However, from the upper side of the HRTEM image as well as the dense regular FFT ED spots in Figure S14(e), twin structures once again appear in the (001) oriented grain as observed in Figure S12 and S13. The parallel lattice fringes as well

as the spotty FFT ED patterns shown in Figure S14(f) reveal a different orientation compared with regions (b)-(e). In contrast to the cases of 883 K and 773 K, the present $Bi_{0.4}Sb_{1.6}Te_3$ nanocolumns display a smaller column size in width and a relatively low density of twinned structures, which might be the reason for its low electrical conductivity.
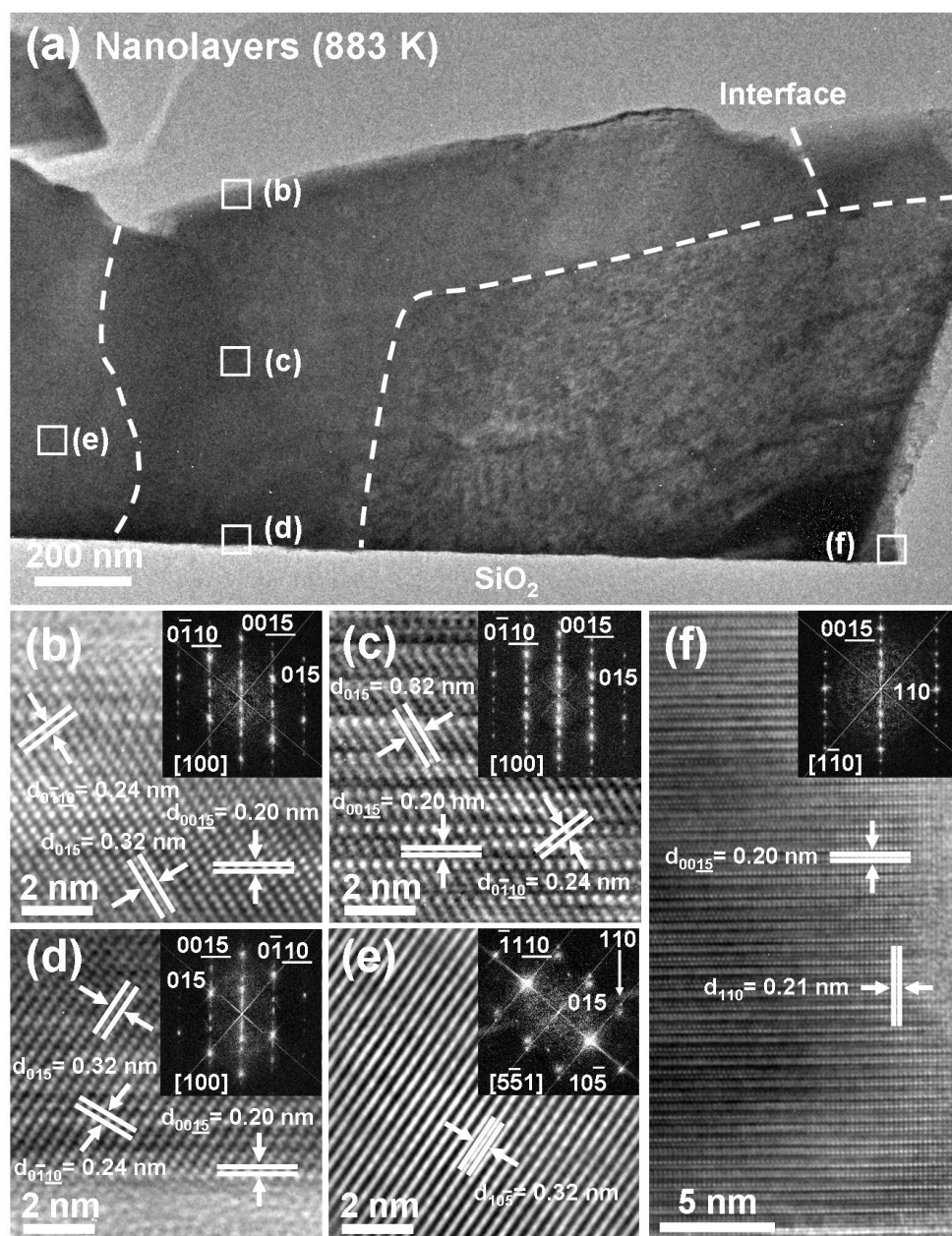
Figure S12. (a) Cross-sectional TEM image of the $Bi_{0.7}Sb_{1.3}Te_3$ nanolayers deposited on SiO_2/Si substrates at 883 K showing film thickness of ~480 nm and obvious interfaces as indexed by dash lines. (b)-(f) The selected regions for HRTEM imaging and the corresponding FFT ED patterns. The zone axis and a few main reciprocal lattice points are indexed.
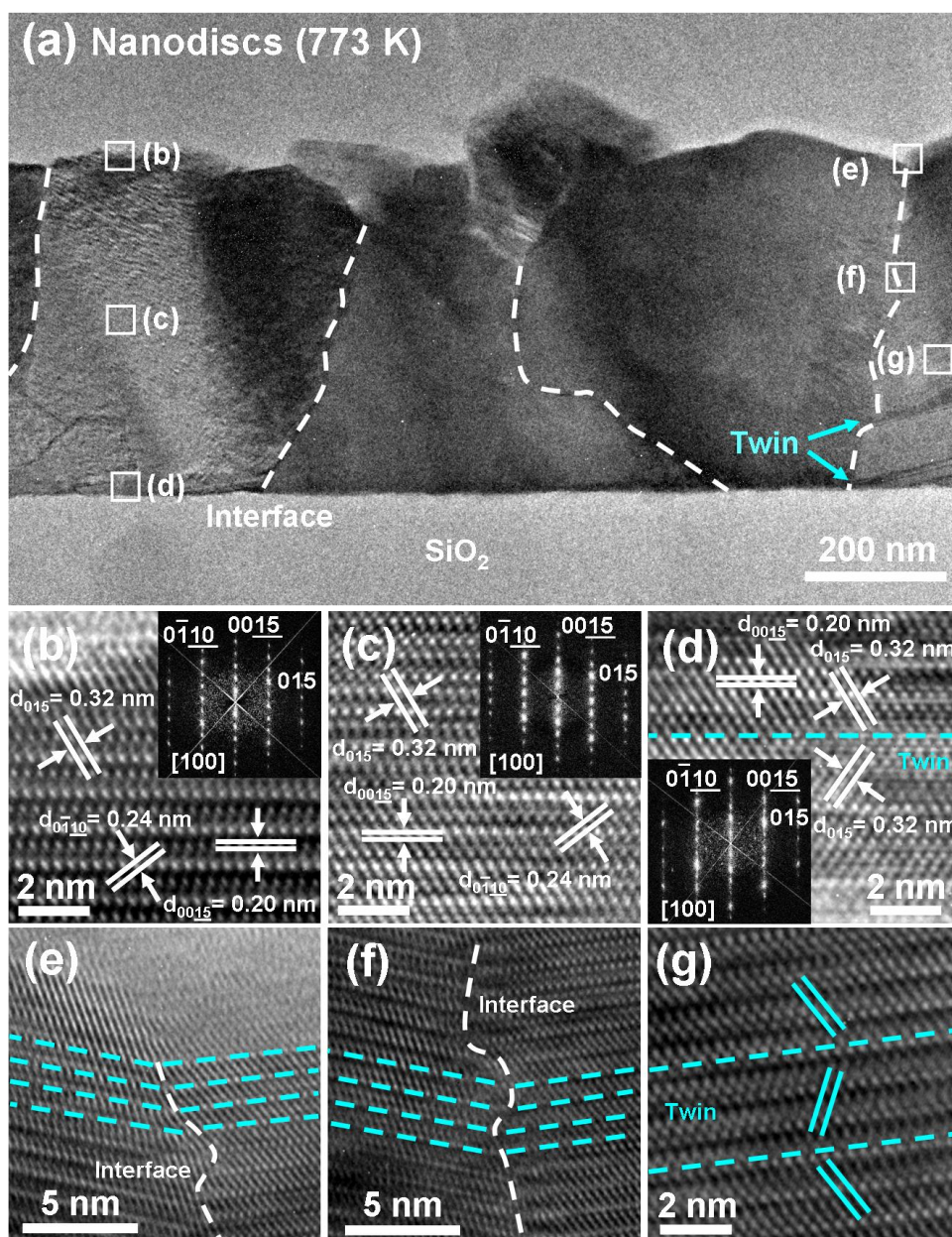
Figure S13. (a) Cross-sectional TEM image of the $Bi_{0.5}Sb_{1.5}Te_3$ nanodiscs deposited on SiO$_2$/Si substrates at 773 K showing a uniform film thickness of ~690 nm and obvious interfaces as indexed by dash lines. (b)-(d) The selected regions for HRTEM imaging and the corresponding FFT ED patterns. The zone axis and a few main reciprocal lattice points are indexed. The HRTEM images of (e)-(f) twin boundaries between neighboring grains and (g) the basal-plane twin band.
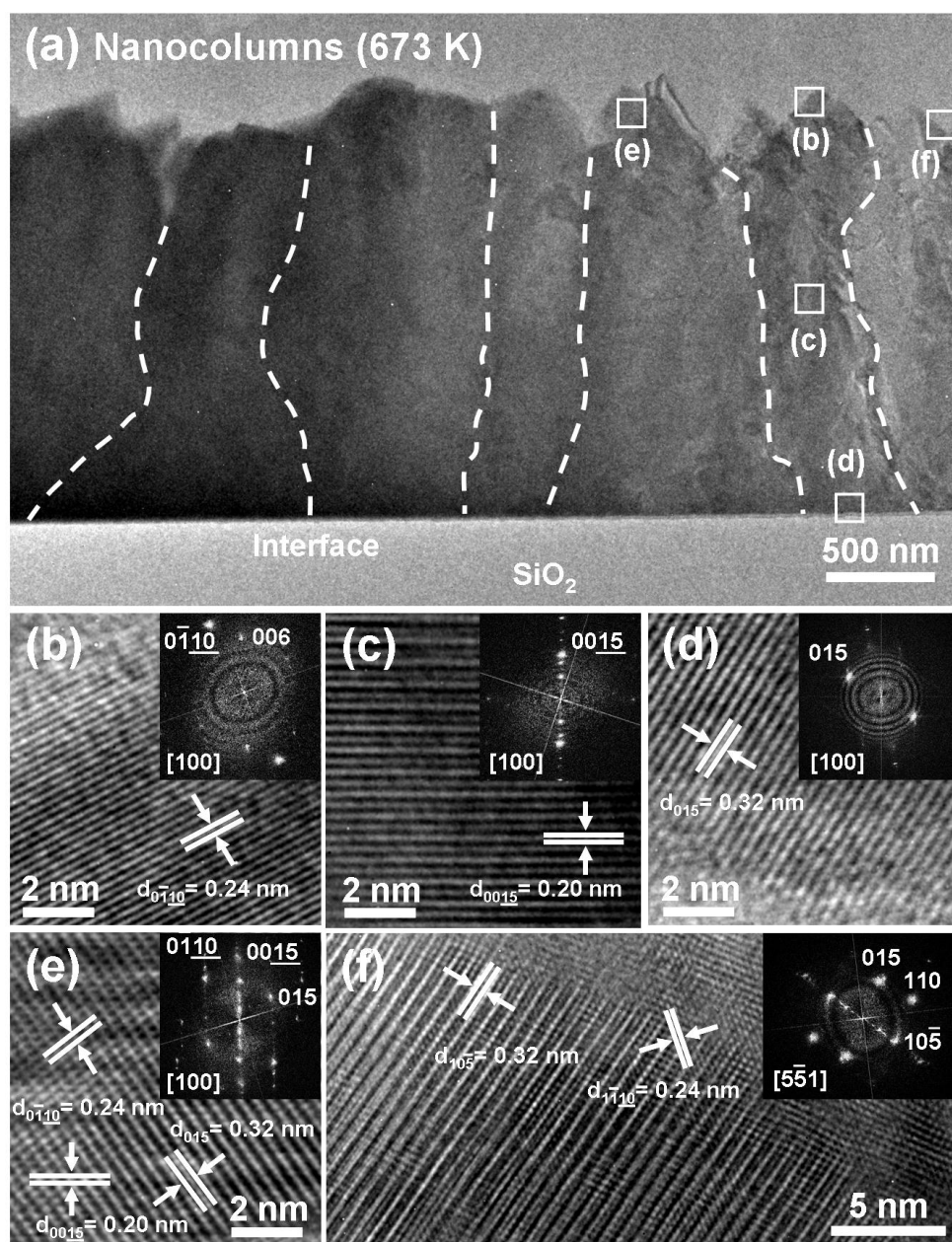
Figure S14. (a) Cross-sectional TEM image of the $Bi_{0.4}Sb_{1.6}Te_3$ nanocolumns deposited on SiO_2/Si substrates at 673 K showing a uniform film thickness of ~1250 nm and obvious interfaces as indexed by dash lines. (b)-(f) The selected regions for HRTEM imaging and the corresponding FFT ED patterns. The zone axis and a few main reciprocal lattice points are indexed.

Microstrain and nanograin size analyses of the most outstanding specimens selected from these three series of Bi$_x$Sb$_{2-x}$Te$_3$ nanostructures

The Williamson-Hall method is expressed by[7,8]

$$\beta \cos(\theta) = \frac{K\lambda}{D_\beta} + 4\varepsilon \sin(\theta) \qquad (1)$$

where β is the full width at half maximum (FWHM) of the selected diffraction peak at 2θ, K is the Scherrer factor (~0.9), λ (~0.15406 nm) is the wavelength of the CuK_α radiation, D_β is the nanograin size, and ε is the microstrain. The ε and D_β can be respectively obtained from the slope and intercept of the linear fitting in the plot of $\beta \cos(\theta)$ versus $4\sin(\theta)$.

Figure S6a shows the Williamson-Hall plot derived from the (006), (015), (10$\underline{10}$), and (00$\underline{15}$) reflections of the Bi$_x$Sb$_{2-x}$Te$_3$ nanoassemblies. The nanograin size and the microstrain obtained are shown in Figure S6b. As shown in Figure S6b, the nanograin size increases with the deposition temperature and the microstrain obtained for these nanoassemblies is smaller than 0.2 %.
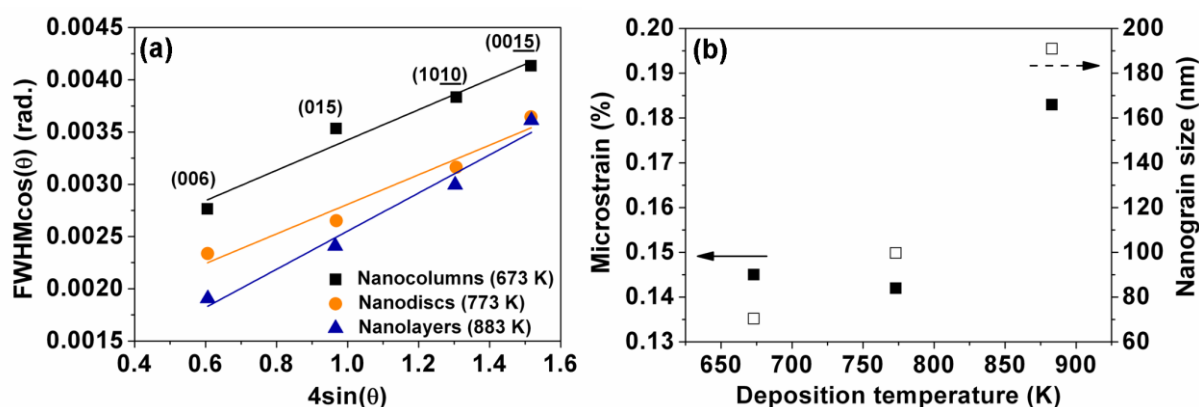
Figure S15. (a) The Williamson-Hall plot for the Bi$_x$Sb$_{2-x}$Te$_3$ nanoassemblies. (b) Microstrain (closed square) and the nanograin size (open square) as a function of the deposition temperature.

References

1. Poudel, B.; Hao, Q.; Ma, Y.; Lan, Y.; Minnich, A.; Yu, B.; Yan, X.; Wang, D.; Muto, A.; Vashaee, D.; Chen, X.; Liu, J.; Dresselhaus, M. S.; Chen, G.; Ren, Z. *Science* **2008**, *320*, 634-638.

2. Russo, V.; Bailini, A.; Zamboni, M.; Passoni, M.; Conti, C.; Casari, C. S.; Bassi, A. L.; Bottani, C. E. *J. Raman Spectrosc.* **2008**, *39*, 205-210.

3. Thornton, J. A. *J. Vac. Sci. Technol.* **1974**, *11*, 666-670.

4. Zhao, Y.; Burda, C. *ACS Appl. Mater. Inter.* **2009**, *1*, 1259-1263.

5. Purkayastha, A.; Kim, S.; Gandhi, D. D.; Ganesan, P. G.; Borca-Tasciuc, T.; Ramanath, G. *Adv. Mater.* **2006**, *18*, 2958-2963.

6. Shi, W.; Zhou, L.; Song, S.; Yang, J.; Zhang, H. *Adv. Mater.*, 2008, **20**, 1892-1897.

7. Williamson, G. K.; Hall, W. H. *Acta Metall.* **1953**, *1*, 22-31.

8. Höche, D.; Schikora, H.; Zutz, H.; Queitsch, R.; Emmel, A.; Schaaf, P. *Appl. Phys. A* **2008**, *91*, 305-314.